Internal Wave Breaking at Concave and Convex Continental Slopes*

SONYA LEGG

Department of Physical Oceanography, Woods Hole Oceanographic Institution, Woods Hole, Massachusetts

ALISTAIR ADCROFT

Earth, Atmospheric and Planetary Sciences, Massachusetts Institute of Technology, Cambridge, Massachusetts

(Manuscript received 8 March 2002, in final form 20 May 2003)

ABSTRACT

Internal wave reflection from a sloping topographic boundary may lead to enhanced shear if the topographic angle to the horizontal is close to that of the internal wave group velocity vector. Previous analytic studies have suggested that shear enhancement is reduced at concave slopes as compared with convex and planar slopes near the critical angle. Here the internal wave reflection from concave and convex slopes that pass through the critical angle is investigated numerically using the nonhydrostatic Massachusetts Institute of Technology General Circulation Model (MITgcm). Overturning, shear instability, and resultant mixing are examined. Results are compared with simulations of wave reflection from planar slopes with angles greater than, less than, and equal to the critical angle. In contrast to the analytic predictions, no reduction in mixing is found for the concave slope as compared with the other slopes. In all cases, stratification is eroded in a band above the slope, bounded at its outer edge by the internal wave characteristic. The difference between numerical and analytic results is caused by the nonlinearity of the numerical calculations, where the finite-amplitude flow leads to generation of upslope-propagating bores for a wide range of topographic slopes around the critical angle.

1. Introduction

Recently the tides have been reexamined as a possible source of energy for diapycnal mixing in the ocean interior (Munk and Wunsch 1998). Evidence from satellite altimetry indicates that as much as 30% of tidal dissipation occurs in the open ocean (Egbert and Ray 2000), a process previously thought to occur almost exclusively on the continental shelf. Much recent activity has therefore been focused on understanding where and how this open-ocean component of tidal dissipation occurs (Bell 1975; Baines 1982; Khatiwala 2003; Llewellyn Smith and Young 2002; St. Laurent and Garrett 2002; Polzin 2004). A particular question of interest for climate studies is how much of the tidal energy is converted into potential energy through diapycnal mixing. In deep water, energy is transferred from the large-scale barotropic tide to small turbulent mixing scales through a series of stages. First baroclinic motions are generated by the barotropic tidal flow over topography. Baroclinic energy is then transferred to smaller scales, leading to wave breaking and mixing, through nonlinear wave–wave interactions or further interactions with topography. In this study we examine only one of these stages—the mixing that results when baroclinic internal tides reflect from sloping topography. A scenario that seems particularly likely to lead to mixing is the reflection of an internal wave from a slope with the same angle to the horizontal θ_c as the internal wave characteristic

$$\tan\theta_c = \frac{k}{m} = \left(\frac{\omega^2 - f^2}{N^2 - \omega^2}\right)^{1/2} = s, \qquad (1)$$

where k is the horizontal wavenumber, m is the vertical wavenumber, N is the buoyancy frequency, f is the Coriolis frequency, ω is the wave frequency (equal to the tidal frequency for internal tides), and θ_c is known as the critical angle. Internal waves preserve their angle to the horizontal upon reflection, so that reflection from slopes near the critical angle given above leads to reflected waves with higher wavenumbers and greater shear (Eriksen 1985; Wunsch 1969). Numerical simulations (Slinn and Riley 1996) and laboratory experiments (Cacchione and Wunsch 1974; Ivey and Nokes 1989) of internal wave reflection from a planar slope at the critical angle have shown mixing near the slope.

In the real ocean a slope is more likely to pass through the critical angle at a point rather than over an extended

* Woods Hole Oceanographic Institution Contribution Number 10688.

Corresponding author address: Dr. Sonya Legg, Department of Physical Oceanography, Woods Hole Oceanographic Institution, MS #21, 360 Woods Hole Road, Woods Hole, MA 02543.
E-mail: slegg@whoi.edu

region. The consequences of a nonuniform slope for internal wave reflection must therefore be considered. A typical steep continental slope has at least two critical points (see Fig. 1a). Around a critical point, the slope may be either concave or convex, where a concave slope has $\theta < \theta_c$ for $h < h_c$ and $\theta > \theta_c$ for $h > h_c$, and vice versa for convex slopes (h_c is the topographic height at the critical point; see Fig. 1). The continental slope in Fig. 1a has both a convex region and a concave region. In an analytical study, Gilbert and Garrett (1989) predicted that reflection from concave slopes near the critical angle will not give rise to the same enhanced shear and mixing as planar and convex slopes because reflected waves from above and below the critical point will destructively interfere, a conclusion also reached by Muller and Liu (2000a,b) in a study of wave scattering from finite-amplitude topography. No laboratory or fully nonlinear numerical studies have yet confirmed these predictions. [Cacchione et al. (2002) suggest that the interaction between the internal waves and sediment tends to favor formation of slopes at the critical angle, but we will only consider rigid slopes here.]

Here we examine numerical simulations of internal wave reflection from variable continental slopes close to the critical angle, in particular comparing planar, convex, and concave slopes. We focus on the curvature over most of the slope. [A ''convex'' slope will have a narrow concave region at the base of the slope (Fig. 1b), while a ''concave'' slope will have a narrow convex region at the top of the slope (Fig. 1c).] We will examine whether the Gilbert and Garrett (1989) prediction of weaker mixing on concave slopes holds for finite-amplitude flows and for realistic continental slopes.

Our motivation is the mixing generated by tides, and so our numerical simulations focus on internal waves at the tidal frequency. However, the wave-breaking processes we examine may occur for internal waves at any frequency between the Coriolis and buoyancy frequencies. None of our results are dependent on the specific frequency of the incident wave.

2. Numerical model and problem configuration

For our calculations we use the Massachusetts Institute of Technology General Circulation Model (MITgcm), a versatile ocean model developed at MIT for use on parallel computers (Marshall et al. 1997). The model integrates the incompressible Boussinesq equations, assuming a linear equation of state:

$$\frac{\partial \mathbf{u}}{\partial t} + \mathbf{u} \cdot \nabla \mathbf{u} + f\hat{\mathbf{k}} \times \mathbf{u} = -\nabla P + b\hat{\mathbf{k}} + \nu_h \left(\frac{\partial^2}{\partial x^2} + \frac{\partial^2}{\partial y^2} \right) \mathbf{u} + \nu_v \frac{\partial^2}{\partial z^2} \mathbf{u}, \quad (2)$$

$$\nabla \cdot \mathbf{u} = 0, \text{ and} \quad (3)$$

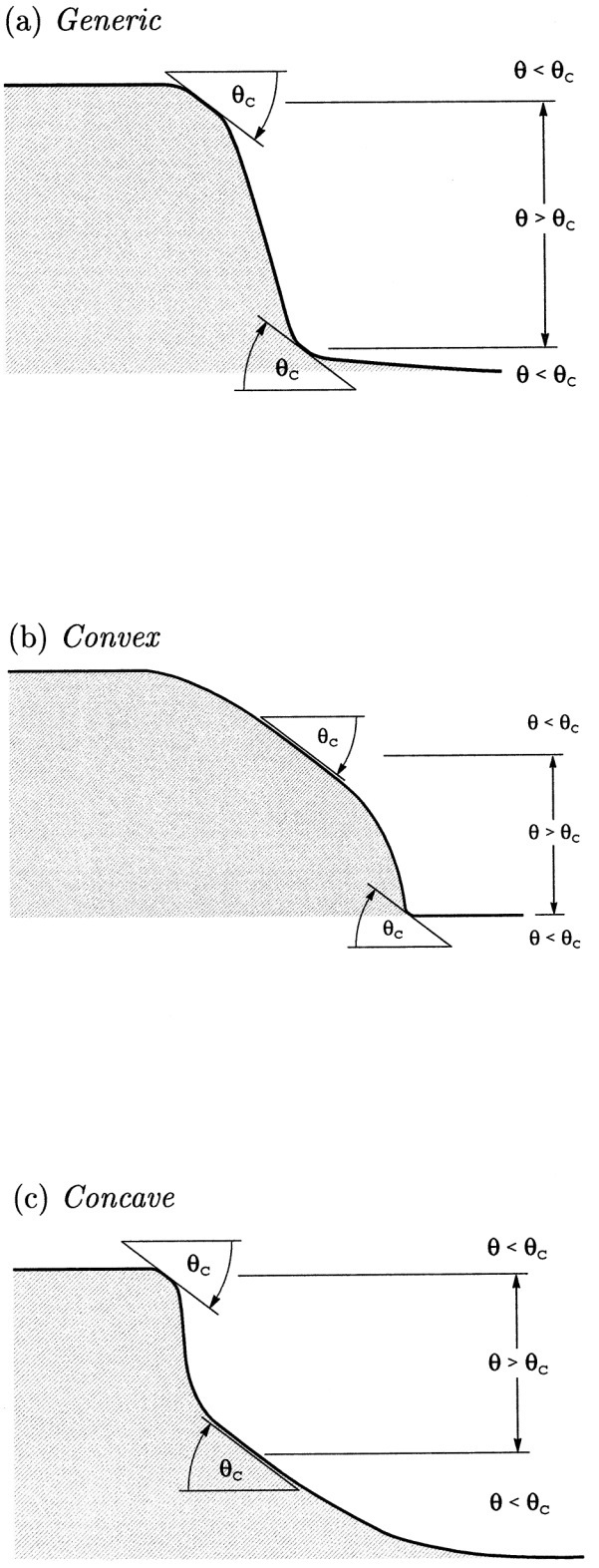

FIG. 1. Schematics of continental slopes, showing the location of the two critical points (where $\theta = \theta_c$). (a) A generic continental slope with a convex critical point at top and a concave critical point below; (b) a ''convex'' slope, for which most of the slope is convex around a midlevel critical point; (c) a ''concave'' slope, for which most of the slope is concave around a midlevel critical point.

$$\frac{\partial b}{\partial t} + \mathbf{u} \cdot \nabla b = \kappa \nabla^2 b, \tag{4}$$

where $\mathbf{u} = (U, V, W)$, the three-dimensional velocity vector; P is the density-scaled pressure; t, x, y, and z are the time and space coordinates; and b is the buoyancy. Here, ν_h and ν_v are the horizontal and vertical viscosity constants, and κ is the tracer diffusivity; $\hat{\mathbf{k}}$ is the unit vector in the vertical direction.

Most of our calculations make use of the model's nonhydrostatic capability, allowing us to explicitly simulate shear instability and overturning processes. We use sufficiently high resolution to explicitly resolve the mixing processes due to Kelvin–Helmholz instability and do not employ a sophisticated subgrid-scale mixing scheme: constant eddy viscosities are used instead, with values of $\nu_h = 10^{-2}$ m s^{-2} and $\nu_z = 10^{-3}$ m s^{-2}. The model employs a direct discretization method with flux limiting for tracers (Pietzrak 1998), preventing the appearance of spurious oscillations in the tracer field and introducing diffusivity where needed for stability. Consequently we can set the explicit diffusivity to zero—that is, $\kappa = 0$—so that the stratification is not eroded in the absence of flow. However, our simulations are not analogous to infinite Prandtl number (where Pr = ν/κ) since in regions of small-scale structure the implicit numerical diffusivity is finite (but variable).

The MIT model represents topography through a finite-volume formulation, allowing arbitrarily small increments in topographic height [to within limits set by the Courant–Friedrichs–Lewy (CFL) criterion; Adcroft et al. 1997]. All of our calculations in this study are two-dimensional, with topography consisting of a flat bottom in the left-hand side of the domain, a sloping region to the right, and finally a continental shelf region to the far right. Initial conditions consist of a stable, horizontally uniform stratification, and no flow:

$$b(t = 0) = N^2 z \text{ and}$$
$$U(t = 0) = V(t = 0) = W(t = 0) = 0, \tag{5}$$

where N is the uniform buoyancy frequency.

The boundary conditions for b are no-flux at top and bottom. Since $\kappa = 0$ this does not lead to an erosion of the initial stratification in the absence of flow. Boundary conditions for the velocity fields are no-slip at the bottom topography (i.e., $u_t = 0$ where u_t is the velocity parallel to the topography) and no-stress at the surface ($\partial u/\partial z = \partial v/\partial z = 0$). There is no flow normal to the topography, while at the surface a linear free surface condition is applied, so that $w_{z=0} = \partial \eta/\partial t$, where η is the free surface height.

At the offshore boundary an internal wave is forced by specifying oscillating velocities and buoyancy anomalies that satisfy the internal wave equations,

$$U(0, z, t) = U_0 \cos(mz) \sin(\omega t), \tag{6}$$

$$V(0, z, t) = U_0 \frac{f}{\omega} \cos(mz) \cos(\omega t), \tag{7}$$

$$b(0, z, t) = N^2 z + U_0 N \left(\frac{\omega^2 - f^2}{\omega^2}\right)^{1/2} \sin(mz) \sin(\omega t), \tag{8}$$

and

$$W(0, z, t) = -U_0 \left(\frac{\omega^2 - f^2}{N^2 - \omega^2}\right)^{1/2} \sin(mz) \cos(\omega t), \tag{9}$$

where ω is the forcing frequency; m is the vertical wavenumber appropriate to a mode-1 internal wave, $m = \pi/H$; U_0 is the velocity amplitude of the forcing; U is the velocity in the x direction (toward the slope); V is the velocity in the y direction (along the slope); and W is the vertical velocity.

These anomalies forced at the boundary lead to an onshore-propagating internal wave of the form

$$U(x, z, t) = -U_0 \cos(mz) \sin(kx - \omega t), \tag{10}$$

where k is given from the dispersion relation in Eq. (1). The oscillation frequency is set to the M_2 tidal frequency: $\omega = 1.41 \times 10^{-4}$ s^{-1}. Since we include the Coriolis frequency in our calculations, the along-slope velocity component (V) of an internal wave propagating normal to the slope is nonzero, and is one-quarter of a period out of phase with the velocity in the cross-slope direction (U). We ramp up the boundary forcing slowly over one tidal period to avoid transients caused by impulsively switching on the forcing.

These boundary conditions do not allow internal waves reflected from the topography to radiate out of the domain. Hence after such time that internal waves might reflect from the topography and be re-reflected at the boundary back into the domain, we can no longer be assured of an internal wave of the pure form given above propagating toward the slope. It may be possible to handle this problem by separating the flow near the boundary into the incoming and outgoing wave components and applying the Orlanski radiation condition to the outgoing component only. However, we did not explore this possibility here and hence focus primarily on the initial flow evolution at the slope, before such contamination might have taken place.

Several nondimensional parameters control the behavior of internal tide–topography interactions. The first is the ratio of the topographic slope to the wave characteristic slope:

$$\alpha = \frac{dh/dx}{(\omega^2 - f^2)/(N^2 - \omega^2)^{1/2}}, \tag{11}$$

where if $\alpha < 1$ the topography is subcritical, if $\alpha = 1$ the slope is critical, and if $\alpha > 1$ the topography is supercritical. As described in the previous section our focus is on topography where $\alpha = 1$ somewhere. Concave slopes have $\alpha > 1$ above the critical point and $\alpha < 1$ below the critical point, and vice versa for convex slopes.

A second nondimensional parameter describes the

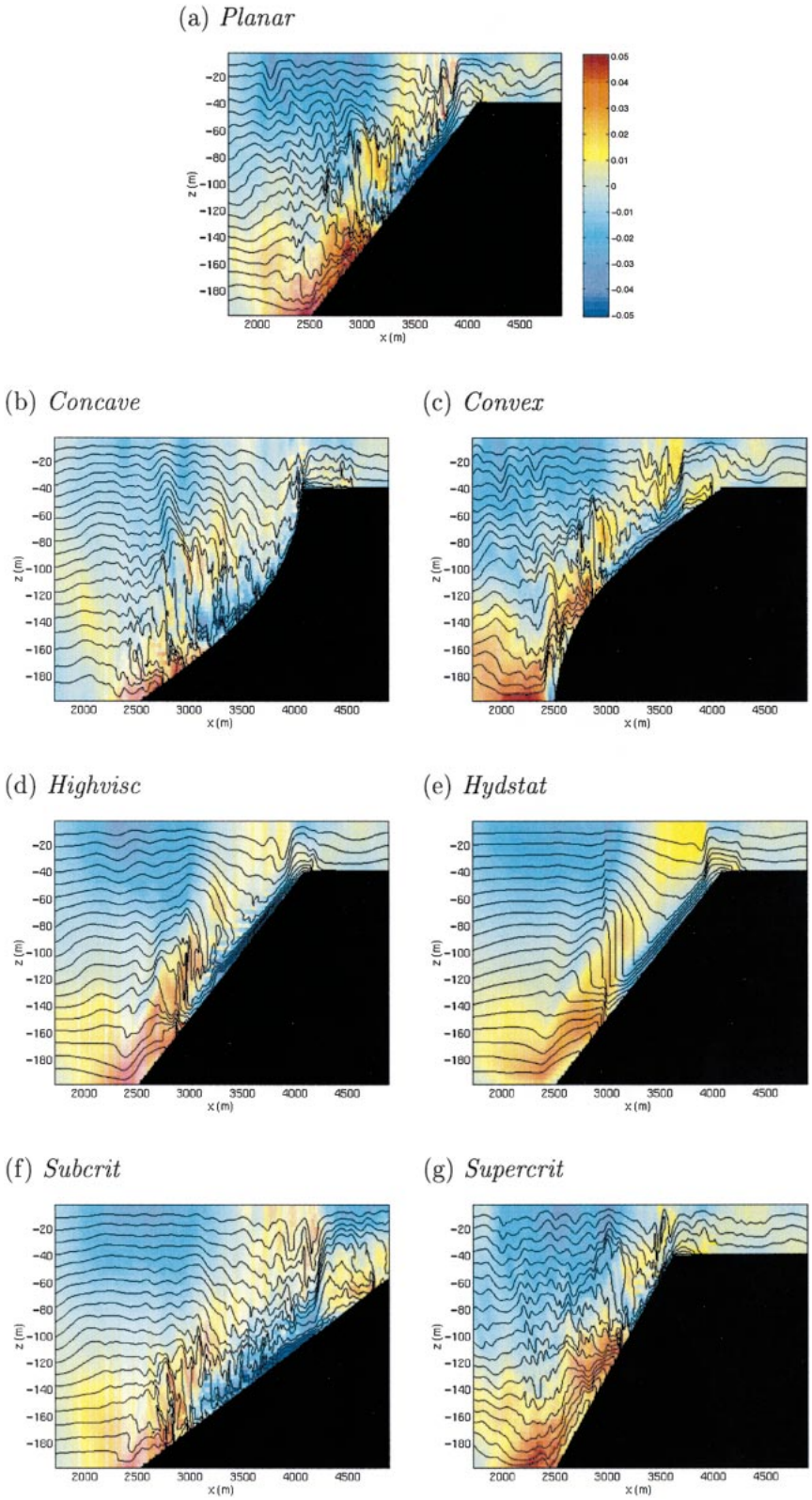

FIG. 2. Snapshots of cross-slope velocity (color) and buoyancy at a time $t = 5.39T$ after the beginning of the calculation. The color scale extends between $U = -0.05$ m s^{-1} (blue) and $U = 0.05$ m s^{-1} (red), and the contour interval is $\Delta b = 9.81 \times 10^{-6}$ m s^{-2}.

nonlinearity of the flow in terms of a wave Froude number:

$$\mathrm{Fr} = U_0/c_p, \tag{12}$$

where U_0 is the amplitude of the internal tide horizontal velocity and c_p is the horizontal component of the phase velocity of the wave. In all of our calculations, Fr is small for the boundary-forced wave, which behaves like a linear internal wave. However, both the internal tide velocity and the phase velocity are modified upon reflection from topography, and so Fr may increase significantly.

All of our experiments have uniform stratification $N^2 = 1 \times 10^{-6}$ s^{-2}, Coriolis frequency $f = 10^{-4}$ s^{-1}, internal wave amplitude $U_0 = 0.024$ m s^{-1}, and gravest vertical mode $m = \pi/H$, where H is the depth of the fluid. The domain size is Lx $\times$ Lz = 13.3 km $\times$ 200 m, with resolution nx $\times$ nz = 640 $\times$ 60; x therefore varies from $x = 0$ to $x = 13.3$ km. The resolution is nonuniform in the x direction, with most grid points concentrated over the sloping topography, where $\Delta x = 7.2$ m and $\Delta z = 3.333$ m. At the left-hand boundary, $x = 0$ where the wave is forced, the fluid has a depth of 200 m, with flat-bottomed topography. At $x = 2.5$ km the slope begins. The 40-m-depth flat shelf begins at $x = 4.08$ km for most calculations The large extent of the shelf (from $x = 4.084$ km to $x = 13.3$ km) ensures that the slope processes are not influenced by the onshore boundary, where Orlanski radiation conditions are applied. Also, N has been chosen to give a horizontal wavelength that is not too large in comparison with the vertical depth, thereby minimizing the disparity in vertical and horizontal resolution.

A third important parameter regarding the slope is the ratio of length scales λ_x/L_h, where λ_x is the horizontal wavelength of the wave and L_h is the horizontal length scale of the slope. For our simulations with a mode-1 internal wave, $\lambda_x = 3.96$ km, and for the critical slope from $h = -200$ m to $h = -40$ m, $\lambda_x/L_h = 2.5$. The slope therefore occupies a little less than one-half of an incoming wave wavelength.

We examine five different slopes. The first, a linear slope (hereinafter referred to as *Planar*), has slope equal to that of the wave characteristic: $dh/dx = s = 0.101$ for our choice of N, ω, and f. Two other slopes are concave (*Concave*) and convex (*Convex*) about the midpoint of the slope, with the slope beginning and ending at the same location as the linear slope, and with critical slope halfway up the slope, at $z = -120$ m. (Note that the ''convex'' slope has a concave corner at the base of the slope, and the ''concave'' slope has a convex corner at the top of the slope.) Then we include a linear subcritical slope, with $dh/dx = 0.06$ (*Subcrit*) and a linear supercritical slope, with $dh/dx = 0.142$ (*Supercrit*).

We also repeat the linear critical slope calculation using a hydrostatic version of the MIT model (*Hydstat*), with implicit convective adjustment (large vertical diffusivity in statically unstable regions) to parameterize vertical mixing. In the hydrostatic calculations horizontal viscosity had to be increased by an order of magnitude relative to the nonhydrostatic calculations to ensure stability, so that $\nu_h = 10^{-1}$ m s^{-2} (ν_v is unchanged). To ensure a clean comparison we therefore also include a nonhydrostatic calculation with the higher value of horizontal viscosity (*Highvisc*), but with vertical mixing explicitly resolved. We therefore consider a total of seven calculations. Each calculation is run for a total of 18 M_2 tidal periods. A quasi–steady state is achieved after about four M_2 tidal periods.

The Reynolds number is given by $\mathrm{Re} = UL/\nu$, where $U = U_0$ and $\nu = \nu_h$ and L is an advective length scale, which for the waves can be estimated as $U_0/\omega = 170$ m. Then Re = 200 for most calculations, or Re = 20 for the high-viscosity calculations. Of course, the Reynolds number is modified on reflection, as the wave amplitude changes.

Final governing nondimensional parameters are the off-normal oblique angle of incidence of the wave, which is held at zero in this study, and the Rossby number $\mathrm{Ro} = U/(fL)$. On the advection scale Ro = 1.4, while on the wavelength scale Ro = 0.06: rotation is important for the wave motion but may not influence the advective motions associated with mixing.

3. Results

a. Qualitative features

To illustrate the qualitative features of the flow when the internal wave reflects from the slope, we show two snapshots, one at $t = 5.39T$ (Fig. 2) and the other at $t = 5.94T$ (Fig. 3) after the beginning of the calculation, for each of the seven cases. Here T is the internal wave period, equal to the M_2 tidal period. At $t = 5.39T$ there is a bore clearly visible in all calculations, located somewhere on the lower to middle part of the slope. The bore consists of a sharp, almost vertical density front adjacent to the slope, separating dense fluid advected up the slope from the less dense fluid into which it is moving. Similar borelike features have been noted in earlier laboratory studies (Ivey and Nokes 1989) and numerical simulations (Slinn and Riley 1996). Analytical studies of finite-amplitude internal wave reflection from near-critical planar slopes predict the symmetry breaking that leads to the formation of these density fronts (Thorpe 1992; Dauxois and Young 1999). The bore is propagating up the slope in all cases. Vertically above the sharpest density gradients, there is a region of overturned isopycnals, characteristic of a breaking wave. This feature is seen in all the nonhydrostatic calculations but not in *Hydstat*. Instead in *Hydstat* statically unstable fluid is immediately homogenized by the convective parameterization, so that vertical isopycnals result instead. The bore is accompanied by convergent flow in the region adjacent to the slope. The downslope flow ahead of the bore is confined to a thinner layer

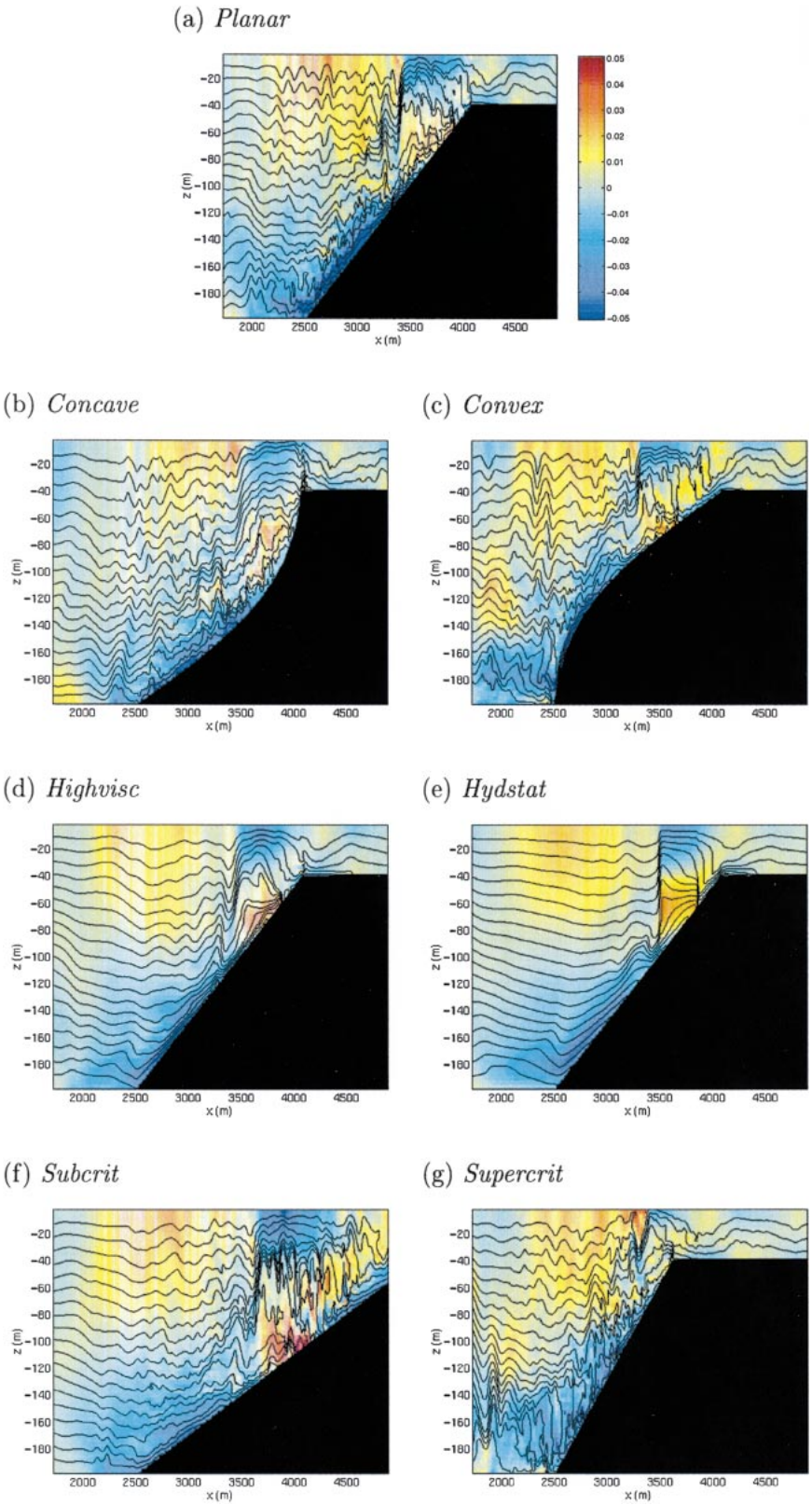

FIG. 3. As for Fig. 2, but for $t = 5.94T$.

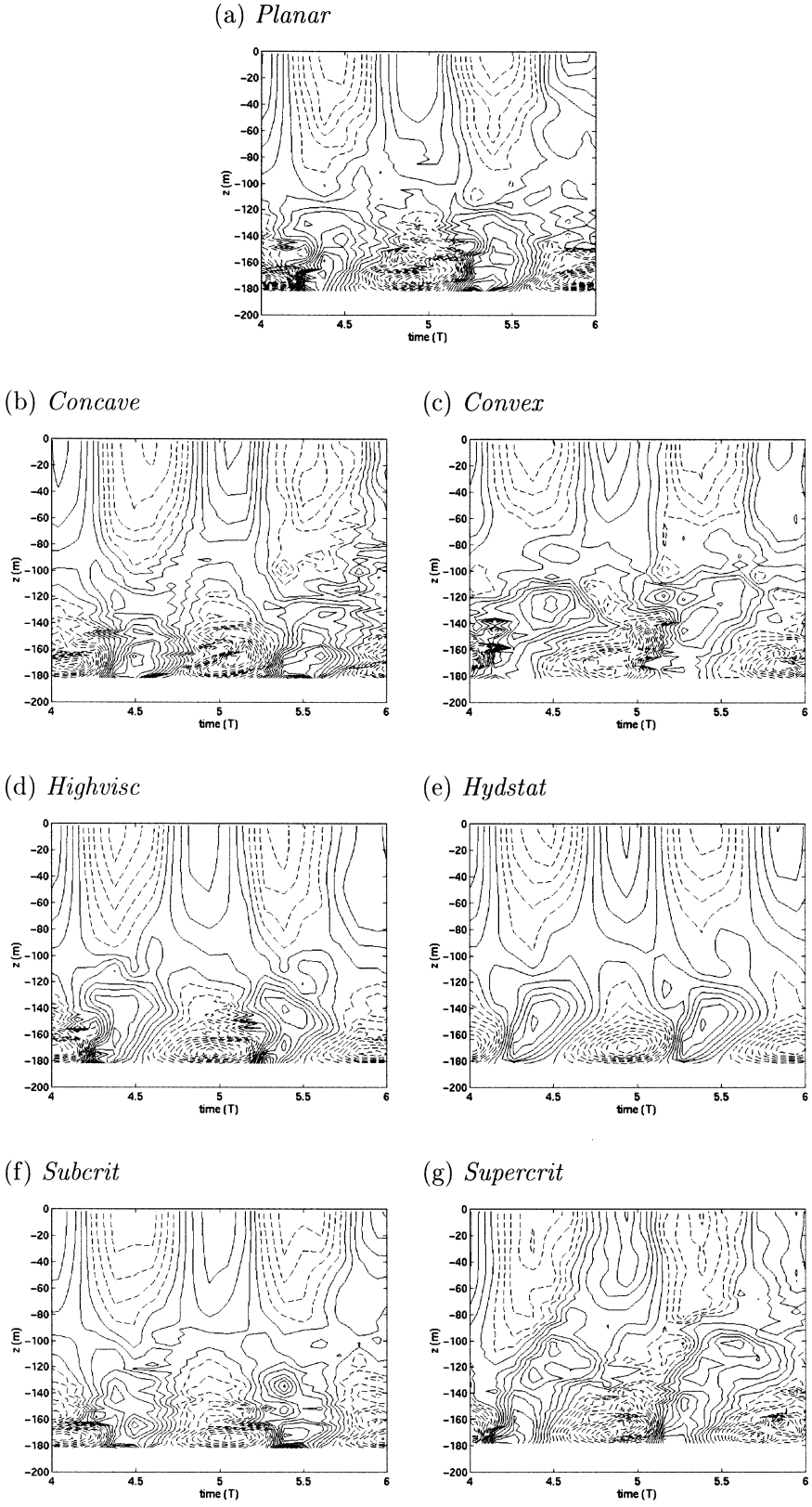

FIG. 4. Time–depth plots of cross-slope velocity U at a location where the topographic height $h = -180$ m. Contour spacing is $\Delta U = 0.005$ m s^{-1}.

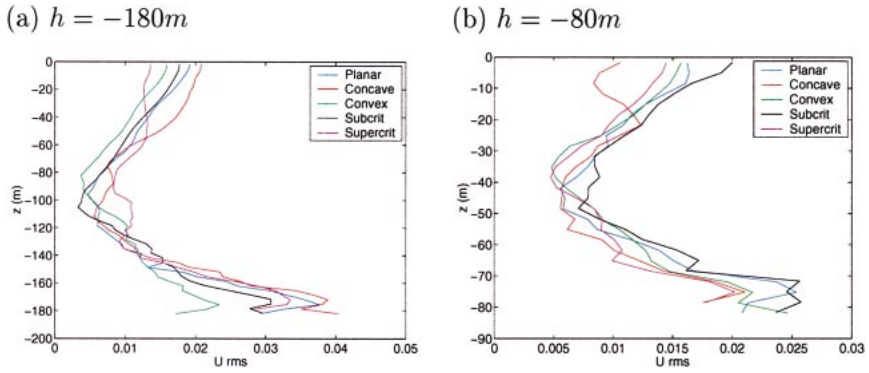

FIG. 5. Profiles of the rms cross-slope velocity as a function of height for topographic depth (a) $h = -180$ m and (b) $h = -80$ m, for planar (blue), concave (red), convex (green), subcritical (black), and supercritical (magenta) slopes.

than the upslope flow and therefore leads to strong shear, resulting in instability and mixing in low-viscosity calculations but not in *Highvisc* or *Hydstat.*

About 0.5 forcing period later, at $t = 5.94T$, the bore has now moved up the slope. In most cases, an accompanying front is seen in upper layers, this time associated with downward depression of the isopycnals. This front, associated with convergent flow above and divergent flow below, is collocated with the rear of the dense bore below and propagates toward shallow water at the same rate as the dense bore. Behind this front, the isopycnals are relatively flat away from the slope, while at the slope the dense fluid that has been carried up the slope is accelerating back down under gravity. The bore in *Concave* is less marked than in the other cases, having disappeared in the steepest part of the slope, and is just reappearing at the shelfbreak corner. *Highvisc* differs from *Planar* primarily in the smoothness of the flow, with less shear instability and mixing, especially in the downslope flow. The hydrostatic calculation *Hydstat* appears to reproduce many of the features of the nonhydrostatic calculation *Highvisc*, but the fronts and bores are more extreme and shocklike.

Note that the nature of the slope—critical, supercritical, subcritical, convex, concave—appears to have relatively little influence on the qualitative features of the flow in this particular regime. All cases show a dense front propagating up the slope, even though the direction of the group velocity of the reflected wave is toward shallower water for subcritical slopes and toward deeper water for supercritical slopes.

Another view of the evolution of the flow can be obtained by examining time–depth plots of the velocity and density fields at specified locations on the slope. We compare profiles taken in the same depth of water (not the same distance on the x axis, because of the different topography). Figure 4 shows cross-slope velocity profiles at water depth of 180 m for two time periods, after a quasi–steady state has been reached. At this depth *Planar* shows enhanced upslope and downslope flow near the bottom, with upslope flow extending slightly higher into the fluid. The flow pattern does not show upward or downward phase propagation, except perhaps for some downward phase propagation visible in the upslope flow at about $z = -130$ m, and slight upward phase propagation below. The *Concave*, *High-*

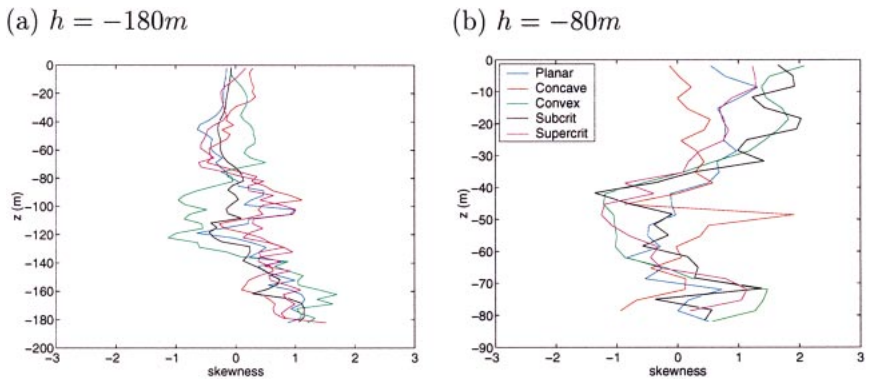

FIG. 6. Profiles of the skewness of the time-derivative of cross-slope velocity as a function of height for topographic depth (a) $h = -180$ m and (b) $h = -80$, for planar (blue), concave (red), convex (green), subcritical (black) and supercritical (magenta) slopes.

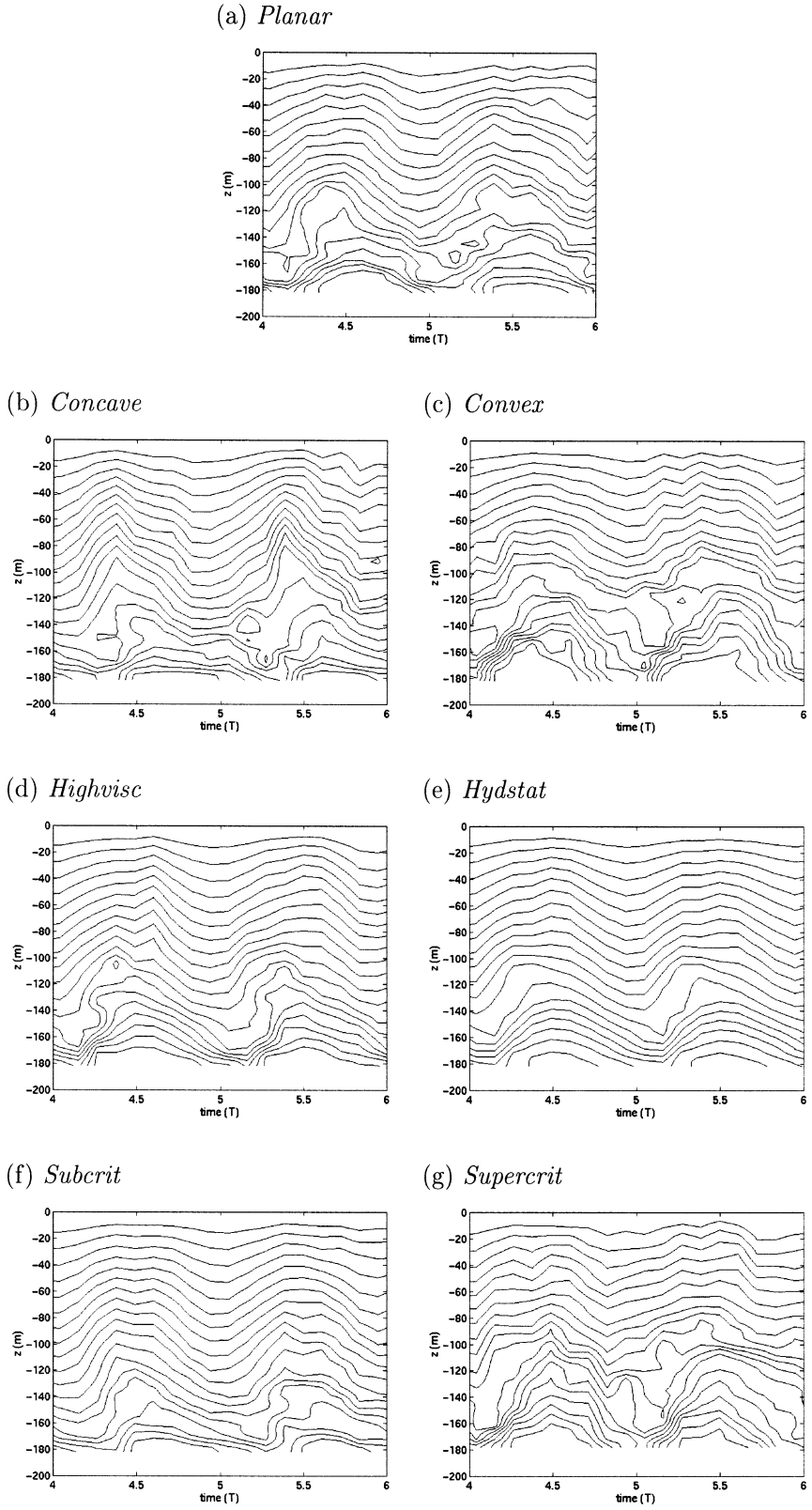

FIG. 7. Time–depth plots of buoyancy b at a location where the topographic height $h = -180$ m. Contour spacing is $\Delta b = 9.81 \times 10^{-6}$ m s^{-2}.

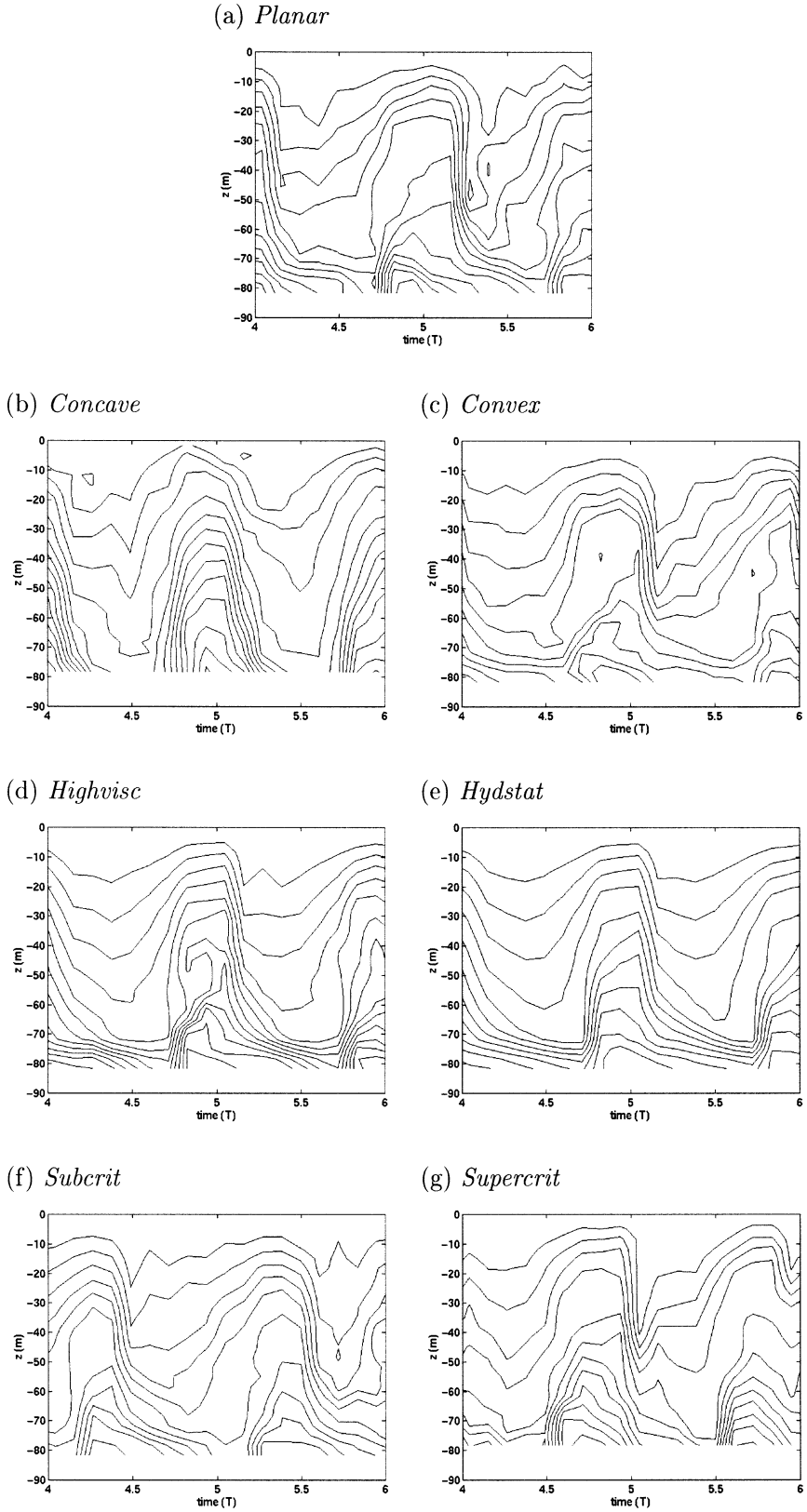

FIG. 8. As for Fig. 7, but for a location where the topographic height $h = -80$ m.

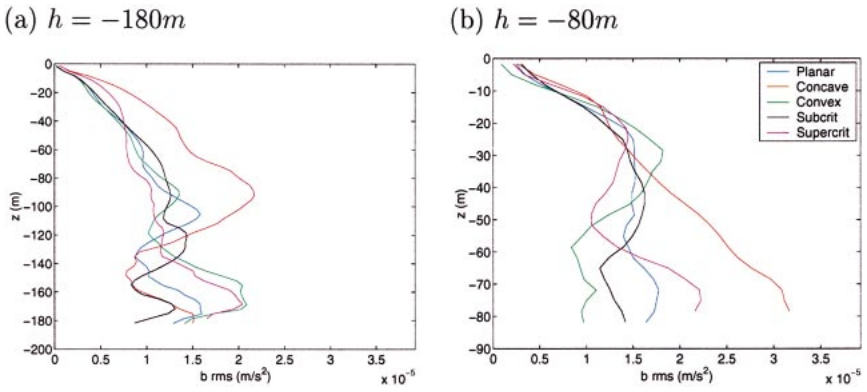

FIG. 9. Profiles of the rms buoyancy as a function of height for topographic depth (a) $h = -180$ m and (b) $h = -80$ m, for planar (blue), concave (red), convex (green), subcritical (black), and supercritical (magenta) slopes.

visc, *Hydstat*, and *Subcrit* cases are all qualitatively similar to *Planar* at this depth (note that *Concave* has subcritical slope at this depth). However, *Convex* and *Supercrit* show a local maximum in the upslope flow at about $z = -120$ to -130 m, displaced above the bottom, and upward phase propagation is pronounced, especially in *Supercrit.* Upward phase propagation indicates downward energy propagation, which would be expected for a wave reflected from a supercritical slope. The bore snapshots (Fig. 2) show that the upslope velocity in the bore, rather than being aligned with the topography on a supercritical slope, is aligned along the wave characteristic slope and hence is displaced slightly above the slope. In the convex case, which is supercritical in water depth of $d = -180$ m, the maximum upslope velocity at $z = -120$ m is therefore the extension of the upslope flow above the critical point at $d = -120$ m. We can quantify these differences in the velocity time–depth plots by examining the profiles of root mean square velocity, shown for all calculations in Fig. 5a, which all show a similar shape, dominated by the gravest vertical mode but with small local maxima for *Convex* and *Supercrit* at middepths. (To avoid crowding we omit the profiles for *Hydstat* and *Highvisc*, but these are very similar to *Planar*.) The skewness of the time derivative of U (Fig. 6a) shows that, for all cases, the flow changes suddenly from downslope to upslope (positive skewness), signifying the passage of the convergence zone associated with the bore on the slope.

The buoyancy time–depth plots at this location on the slope, $d = -180$ m (Fig. 7) all show dense fluid displaced up-slope, with strongest density fronts in *Convex* and *Supercrit* and weakest in *Concave* and *Subcrit.* This is quantified in the root mean square buoyancy profiles (Fig. 9a); near the boundary, *Convex* and *Supercrit* have the largest values of b_{rms}, and *Concave* and *Subcrit* have the smallest, while at upper levels *Concave* has the greatest b_{rms}. The passage of the bore, with sudden changes from less dense to denser fluid, is shown by the negative skewness in all cases for db/dt (fig. 10a). This skewness is predicted by weakly nonlinear analytical studies (Thorpe 1992; Dauxois and Young 1999). Similar magnitude negative skewness of the temperature time derivative has been observed near topography by

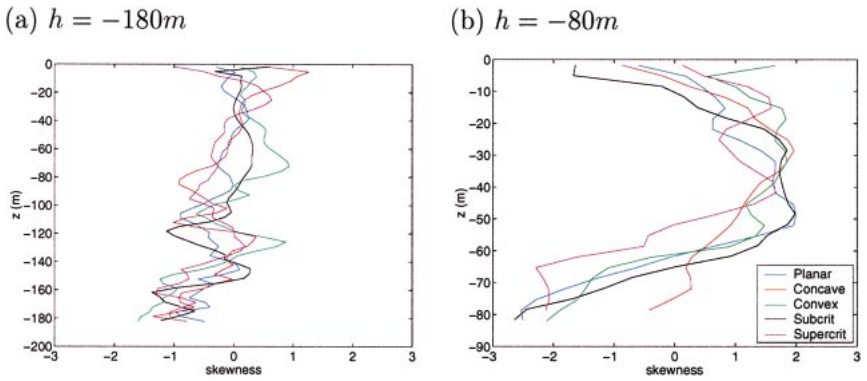

FIG. 10. Profiles of the skewness of the time-derivative of buoyancy as a function of height for topographic depth (a) $h = -80$ m and (b) $h = -80$ m, for planar (blue), concave (red), convex (green), subcritical (black), and supercritical (magenta) slopes.

Thorpe et al. (1991), who propose fronts generated by reflecting internal waves as the likely cause.

Higher up the slope, at $d = -80$ m (Fig. 8), most cases show both upper- and lower-level density fronts, with sudden increases in density at the topography, followed by sudden decreases in density in upper layers. The exception is *Concave,* which shows more symmetrical changes in density. This is quantified by the skewness of the time derivative of buoyancy, which is negative near the bottom boundary (passage of a dense front) for all cases (Fig. 10b) except *Concave,* which has skewness close to zero. *Concave* does, however, have significantly larger b_{rms} at this fluid depth than the others (Fig. 9b). At this depth the cross-slope velocity signal is less coherent (as shown by the skewness of the time derivative, which does not show any identifiable pattern; Fig. 6b) and U_{rms} is similar for all cases (Fig. 5b).

Our calculations therefore show that there is a similarity between all calculations when the slope is subcritical or critical. Even when the slope is supercritical many of the same qualitative features may be found, with a bore propagating up the slope. However, the upslope flow is aligned along the wave characteristic, displacing it off the slope behind the bore in the supercritical cases (*Supercrit* and *Convex* below $d = -120$ m). Near the top of the concave slope qualitatively different behavior is found. When the bore reaches this steep slope (steeper than *Supercrit*), the motion is forced to become more vertical, leading to large-amplitude but symmetric buoyancy oscillations, rather than the asymmetric bores seen on the other slopes.

b. Net changes in stratification

Having demonstrated that qualitative differences in the flow are confined locally to the regions of steep supercritical slope, we now consider how the slope curvature affects the mixing, indicated by changes in stratification. We must bear in mind, however, that mixing in two-dimensional calculations such as these may differ from that in three-dimensional calculations and the real three-dimensional ocean. The process of wave breakdown into turbulence is known to be more efficient and rapid in three dimensions, and mean alongslope currents established through the wave breaking might significantly modify the mixing in three dimensions. Nonetheless, we present the mixing diagnostics here as a reference with which future three-dimensional calculations can be compared and as a qualitative guide to the effects of slope curvature on mixing.

Figure 11 shows the net change in vertical buoyancy stratification defined as follows:

$$\Delta N^2 = \frac{\partial}{\partial z}\left(\frac{1}{T}\int_{t2}^{t2+T} b\, dt\right) - \frac{\partial}{\partial z}\left(\frac{1}{T}\int_{t1}^{t1+T} b\, dt\right), \quad (13)$$

where T is the tidal period and $t1 = 2.5T$ and $t2 = 7.5T$; $t1$ is just before the mixing begins and $t2$ is nearly halfway through the calculation. (As will be seen below, relatively little mixing occurs in the second half of the calculation.) *Planar* shows a broad band of reduced stratification running parallel to the slope, bounded by increased stratification both away from the slope and in a thin zone on the slope. In both *Concave* and *Convex* the increased stratification at the slope is found only where the slope is subcritical, and the band of increased stratification away from the slope is not parallel to the slope, but aligned with the wave characteristic slope. In both *Concave* and *Convex* the mixing is less well organized near the supercritical slope. *Highvisc* is similar to *Planar,* but with a slightly thinner band of modified stratification, less reduction in stratification farther down the slope, and more marked increase in stratification at the slope. *Hydstat* has less stratification increase in the band away from the slope. There is not much mixing on the lower part of the slope. The hydrostatic calculation therefore appears to simulate the mixing less successfully than the propagating bores. This inability to reproduce the mixing cannot be attributed entirely to the absence of shear instability, since this is also absent in *Highvisc. Highvisc* does capture overturning in the head of the bore that *Hydstat* cannot. *Subcrit* shows similar features to *Planar,* with the band of increased stratification aligned with the wave characteristic. *Supercrit* has many similar features, but the zones of reduced and increased stratification appear less well organized.

The time evolution of the stratification is shown in Fig. 12 for the *Planar, Concave, Convex, Highvisc,* and *Hydstat* calculations as a time–depth contour plot located near the bottom of the slope ($d = -120$ m). In each case the stratification change has been calculated from the density field averaged over one tidal cycle, and there is some aliasing due to the relative infrequency with which fields are analyzed (nine times per tidal cycle).

In *Planar* after about seven tidal periods, the stratification reaches an approximate steady state. Both the weakened stratification and the increased stratification above remain at the same height above the boundary, without any further noticeable changes. The region of increased stratification on the slope becomes somewhat thinner and more intermittent. Similar features are seen in *Concave* and *Convex* (and in *Subcrit* and *Supercrit* too, but not shown), but with different depths of the ''mixed'' layer. *Highvisc* has a much thinner region of modified stratification, with a proportionately wider region of increased stratification on the slope, and thinner and more intermittent region of increased stratification above. *Hydstat* is qualitatively different from all the others, with a thick layer of increased stratification near the slope, little decrease in stratification above, and barely any increase in stratification above that. Hence the

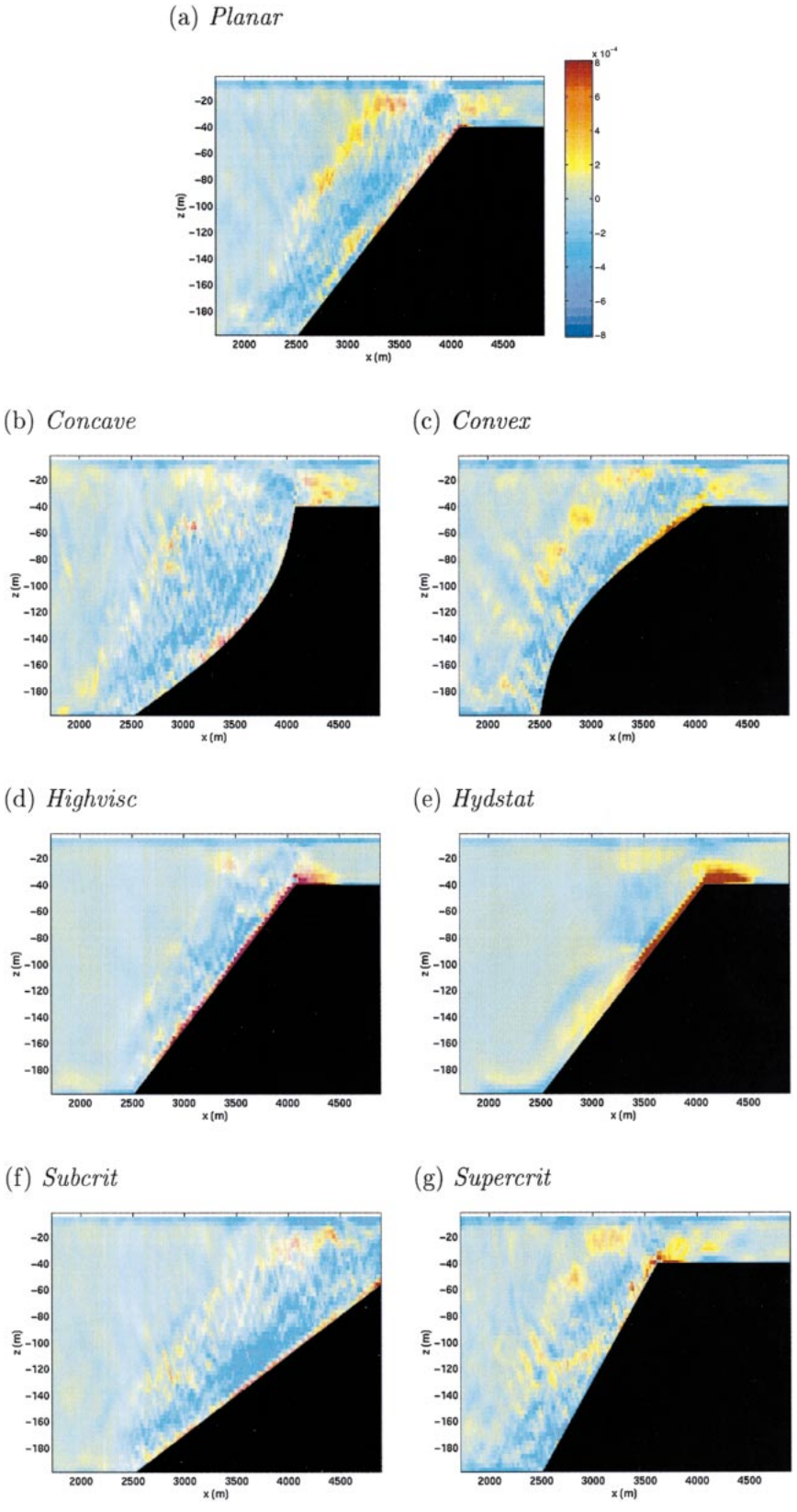

FIG. 11. Snapshots of the change in buoyancy stratification over five tidal periods. The color scale extends from $\Delta N^2 = -1.56 \times 10^{-6}\ \mathrm{s}^{-2}$ (blue) to $1.56 \times 10^{-6}\ \mathrm{s}^{-2}$ (red), with values close to 0 in green.

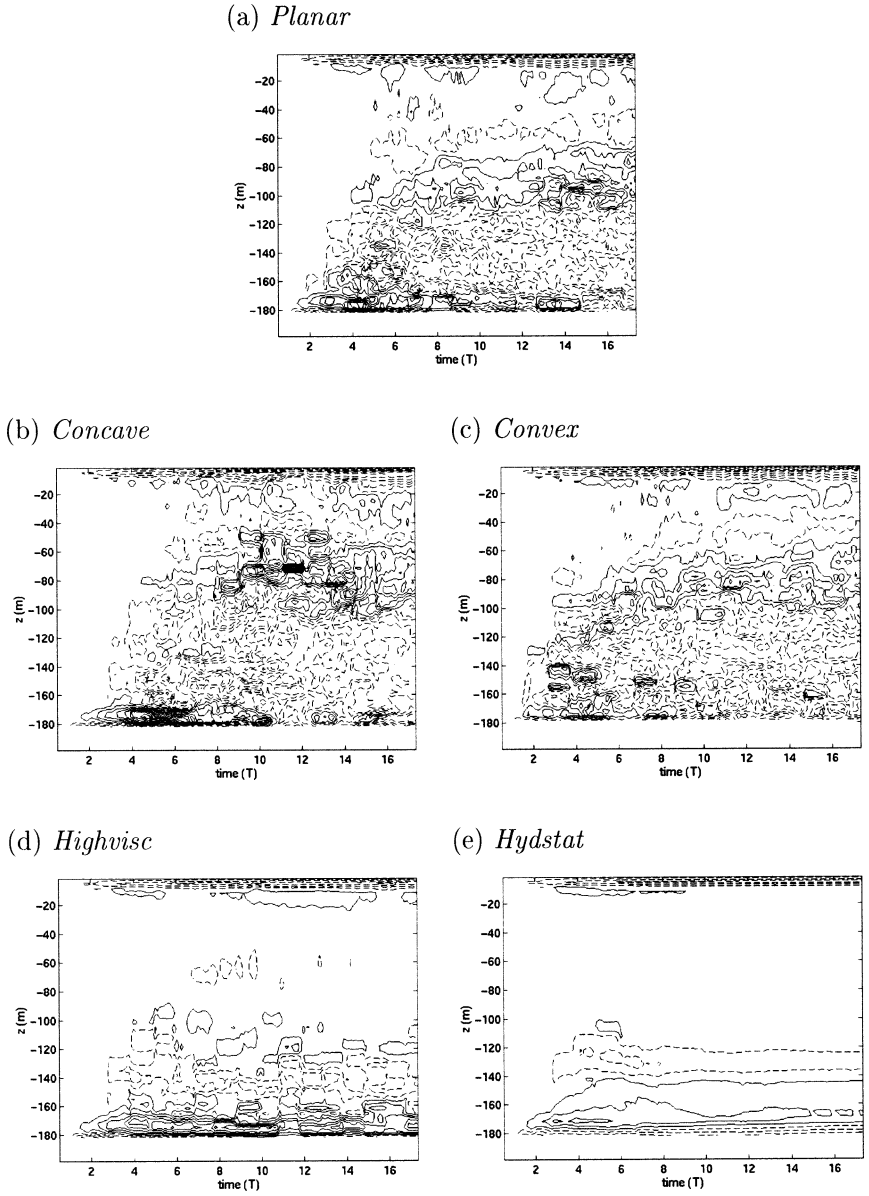

FIG. 12. Depth–time plots of the change in stratification $db/dz - db/dz(t = 0)$ for (a) *Planar*, (b) *Concave*, (c) *Convex*, (d) *Highvisc*, and (e) *Hydstat*. Contour spacing is $\Delta db/dz = 2 \times 10^{-7}$ s^{-2}.

differences in stratification changes seen in Fig. 11 persist for the whole length of the integration.

For comparison the final stratification profile for all of these five cases is shown in Fig. 13. The three low-viscosity cases (*Planar, Concave, Convex*) all have very similar profiles, while the *Highvisc* profile has weaker anomalies confined to a shallower depth, and the *Hydstat* profile is completely different from the rest, especially near the topography. The minimum stratification in *Planar,* although only a small fraction of its initial value, is still nowhere near zero and is considerably greater than ω^2. Hence mixing has not ceased simply because the fluid is already completely mixed. The cessation of mixing seen in these experiments may indicate that the reduction in stratification has in some way modified the wave-breaking process so that mixing no longer occurs. Another possibility is that the incoming wave is corrupted by waves that have been successively reflected from the topography and the offshore boundary, so reducing the internal wave signal near the slope. (This would be expected to be a problem particularly for the concave and supercritical planar slopes, yet the end state for the concave case stratification is very similar to that for the planar and convex cases.) Even if the cessation of mixing is real, and not an artifact of the offshore boundary conditions, it is possible that in three dimen-

sions a different result might be obtained—a steady state could be established by three-dimensional processes such as secondary circulations, baroclinic instability, lateral eddy fluxes, and so on, so that the net mixing to be expected in the ocean cannot be deduced from the transient mixing seen here.

c. Energy budgets and mixing efficiency

In the MIT model, which has a linear free-surface representation, the kinetic energy equation is given by

$$\frac{\partial}{\partial t}K + \boldsymbol{\nabla}\cdot\left(K + \frac{p}{\rho_0} + g\eta\right)\mathbf{u} + \nu\nabla^2 K - wb + \nu\nabla\mathbf{u}\cdot\nabla\mathbf{u} = 0, \tag{14}$$

where $K = (\mathbf{u}\cdot\mathbf{u})/2$, η is the free-surface elevation, b is the buoyancy, p is the pressure, and ν is the viscosity. The term wb represents transfer between kinetic and potential energy. If we integrate this over a volume V defined by $z = -H \rightarrow z = 0$, and $x = x1 \rightarrow x2$, we have

$$\underset{1}{\frac{\partial}{\partial t}\int_V K\,dV} = \underset{2}{-\left(\int_{-H}^{0} Ku\,dz\right)_{x=x1}^{x=x2}} \underset{3}{-\left[\int_{-H}^{0}\left(\frac{p}{\rho_0} + g\eta\right)u\,dz\right]_{x=x1}^{x=x2}} \underset{4}{-\left(\int_{-H}^{0}\nu\frac{\partial K}{\partial x}\right)_{x=x1}^{x=x2}} \underset{5}{-\left[\int_{x1}^{x2}(K + g\eta)w\,dx\right]_{z=0}} + \underset{6}{\int_V wb\,dV} \underset{7}{-\int_V \nu\boldsymbol{\nabla}\mathbf{u}\cdot\boldsymbol{\nabla}\mathbf{u}\,dV}, \tag{15}$$

where term 1 is the kinetic energy tendency, 2 is the kinetic energy advection term, 3 is the pressure transport term, 4 is the diffusive transport term, 5 is the transport at the top surface (only nonzero because we do not have a rigid lid at $z = 0$), 6 is the potential energy conversion term, and 7 is the dissipation term. The companion potential energy equation is

$$\frac{\partial}{\partial t}\Phi + \boldsymbol{\nabla}\cdot\Phi\mathbf{u} + wb = 0, \tag{16}$$

where $\Phi = -zb$, the potential energy. Again we integrate over a volume defined as above to obtain

$$\underset{1}{\frac{\partial}{\partial t}\int_V \Phi\,dV} = \underset{2}{-\left(\int_{-H}^{0}\Phi u\,dz\right)_{x=x1}^{x=x2}} \underset{3}{-\int_V wb\,dV}, \tag{17}$$

where term 1 represents the potential energy tendency, 2 is the potential energy advection, and 3 is the transfer of potential energy to kinetic energy. Now we evaluate the energy budgets for the various numerical simulations, using $x1 = 2.16$ km and $x2 = 4.34$ km so that the whole of the slope and a little of the surrounding flat-bottomed regions are contained within the volume. We confine our examination of the budgets to the region over the slope, thereby avoiding the question of the work done by the boundary forcing. (In particular the work done by the boundary forcing may not be constant since there may be contamination by waves re-reflected from the offshore boundary.)

The potential energy tendency for *Planar* (Fig. 14) is dominated by the internal wave oscillations and is largely balanced by the flux of potential energy into the region from the boundary (there is little flux out of the region onto the shallow slope). However, there is a finite net flux of potential energy into the region, when averaged over a tidal cycle, that is not compensated by a corresponding rise in potential energy and therefore must be balanced by a transfer of potential energy to kinetic energy. Hence the net, tidally averaged, buoyancy flux shown in Fig. 14 in the region over the slope is positive. This is true for all cases except *Supercrit*, which has a buoyancy flux that is highly variable but averages close to zero.

In the tidally averaged kinetic energy budgets (Fig. 15) the pressure transport and potential energy conversion terms (for most cases) supply kinetic energy to the region. The kinetic energy initially rises steeply, but thereafter reaches a quasi–steady state, when dissipation balances the energy inputs by the pressure transport and potential energy conversion. Other terms in the kinetic energy budget are small. In most cases a quasi–steady state is reached after about five tidal periods, including for *Hydstat* and *Highvisc* (not shown). However, *Concave* shows a decline in pressure transport matched by a decline in dissipation toward the end of the calculation and fluctuations in kinetic energy level that continue throughout the calculation (perhaps caused by the contamination of the incoming wave by waves that have been successively reflected from the topography and offshore boundary).

The net positive buoyancy flux arises from the propagation of buoyancy anomalies—the incoming wave—which then break, releasing their potential energy to kinetic energy. Some of the kinetic energy generated during the wave breaking may be converted back to potential energy through mixing of the basic stratifi-

cation. This pathway for loss of kinetic energy cannot be quantified by examining the total budgets. Winters and D'Asaro (1996) show that many oceanic mixing scenarios are associated with both an adiabatic and a diabatic component of buoyancy flux, which may have opposite signs as in this case. Here we attempt to deduce that part of the buoyancy flux that is responsible for mixing by examining the net change in the tidally averaged buoyancy field, assuming in the absence of diffusion or horizontal fluxes,

$$\frac{\partial b}{\partial t} = \frac{\partial}{\partial z}\langle w'b'\rangle. \tag{18}$$

This component of the buoyancy flux can be evaluated by integrating the net change in tidally averaged buoyancy with depth. Since vertical buoyancy flux is zero near the top surface, but nonzero at the sloping topography, we start the integration from the top:

$$\langle w'b'\rangle_t(x, z) = \int_z^0 \frac{1}{t2 - t1}\left[\frac{1}{T}\int_{t2}^{t2+T} b(x, z, t)\, dt - \frac{1}{T}\int_{t1}^{t1+T} b(x, z, t)\, dt\right] dz. \tag{19}$$

As for the stratification shown in Fig. 11 we use $t1 = 2.5T$ and $t2 = 7.5T$, thereby concentrating on the earlier part of the calculation during which mixing of stratification is most active. The time-averaged buoyancy flux responsible for mixing is shown as a function of x and z in Fig. 16. In all cases, negative buoyancy flux (down gradient flux) is localized over the slope. In the low-viscosity cases, it is localized over the center of the slope, where both the slope is critical and the mode-1 internal wave displacements are greatest. In *Highvisc* and *Hydstat* the buoyancy flux is higher up the slope. This would reflect the qualitative observation that the higher-viscosity cases do not include sufficient shear instability, which tends to be the principal mechanism for mixing lower down the slope, whereas the bore, which is represented by both *Highvisc* and *Hydstat* as well as the other calculations, is responsible for most mixing higher up the slope. These values of downgradient buoyancy flux suggest a local eddy diffusivity on the order of $\kappa \sim 10^{-3}\ \mathrm{m^2\ s^{-1}}$.

We have previously shown the kinetic energy dissipation averaged over the region over the slope (Fig. 15). The spatial distribution of the total kinetic energy dissipation, time-averaged over the period $t2 - t1$, is shown in Fig. 17. In all cases dissipation is highest close to the slope in the frictional bottom boundary layer. There is a band of high dissipation bounded by a line roughly parallel to the wave characteristic, but slightly narrower at the bottom of the slope in *Planar*, and considerably narrower in *Highvisc*. In *Concave* the highest dissipation near the slope is not as marked, and instead there is a broader region of high dissipation at the bottom of the slope (the subcritical part of the slope). *Hydstat* has lower magnitude of dissipation than the other cases with the shocklike bores associated with the hydrostatic dynamics responsible for a large fraction of the total. In general the dissipation distribution differs from the buoyancy flux in that it is less localized to a particular area of the slope, and it is enhanced right near the boundary, whereas the buoyancy flux maximum is slightly displaced to the fluid interior, where reductions in stratification are concentrated.

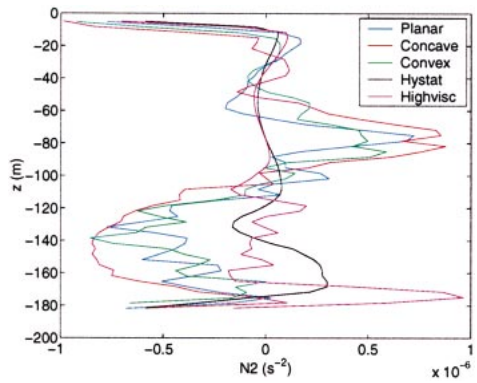

FIG. 13. Profiles of the change in stratification for *Planar* (blue), *Concave* (red), *Convex* (green), *Hydstat* (black), and *Highvisc* (magenta) calculations at the completion of all computation.

Laboratory experiments of reflection of an internal wave beam (Ivey et al. 2000) show a mixing region of depth

$$h = K\lambda_p = K\frac{2\pi}{\sqrt{(k^2 + m^2)\cos(\beta + \theta)}}, \tag{20}$$

with dissipation averaged over this layer (assuming all incoming wave energy is dissipated):

$$\epsilon = \frac{U_0^2\omega \sin[2(\beta + \theta)]}{8\pi K \cos^2(\beta)}, \tag{21}$$

where λ_p is the wavelength of the incoming wave in the

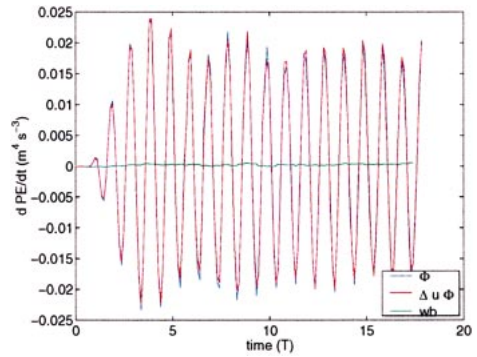

FIG. 14. Time series of the potential energy budget terms for the region over the slope for *Planar*. Shown are the instantaneous potential energy tendency (blue), the instantaneous potential energy transport (red), and the tidally averaged conversion to kinetic energy (green).

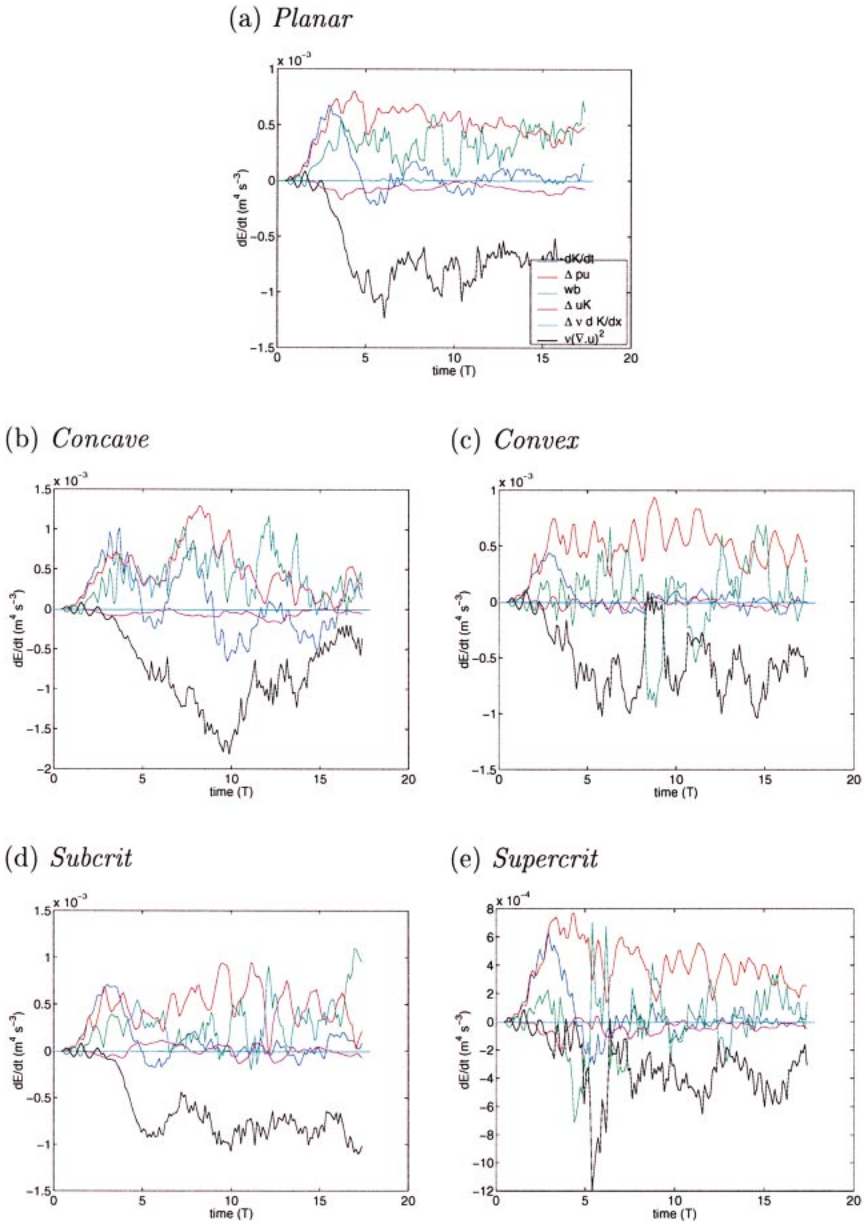

FIG. 15. Time series of the tidally averaged kinetic energy budget terms for the volume over the slope for (a) *Planar*, (b) *Concave*, (c) *Convex*, (d) *Subcrit*, and (e) *Supercrit*. *Highvisc* and *Hydstat* are not shown, but are very similar to *Planar*. Shown are kinetic energy tendency (blue), pressure transport (red), dissipation (black), potential energy conversion (green), advective transport (magenta), and diffusive transport (cyan).

direction normal to the slope and K is a constant, found empirically to be $K \sim 0.1$–0.15; β is the angle of the wave characteristic to the horizontal [$s = \tan(\beta)$], and θ is the angle of the topography to the horizontal. For our parameters. Eq. (20) gives a lower limit of $h \sim 40$ m for the critical planar slope, and Eq. (21) predicts $\epsilon \sim 10^{-8}\ \mathrm{m^2\ s^{-3}}$ for the critical slope, both of which agree favorably with our simulated dissipation layer. Note, however, that Eq. (20) does not account for the variation in depth seen both in noncritical planar slopes and near-critical concave and convex slopes. Nonetheless, the reasonable agreement between the laboratory-derived empirical models and the numerical simulations gives some confidence in these simulations despite their restriction to two dimensions.

We can estimate the mixing efficiency, $\Gamma = \langle w'b' \rangle / \epsilon$, from the time-averaged dissipation and mixing component of buoyancy flux, averaged over the region over the slope. We find $\Gamma = 0.02$ (*Hydstat* and *Highvisc*)–0.095 (*Concave*). *Convex* and *Planar* have similar Γ,

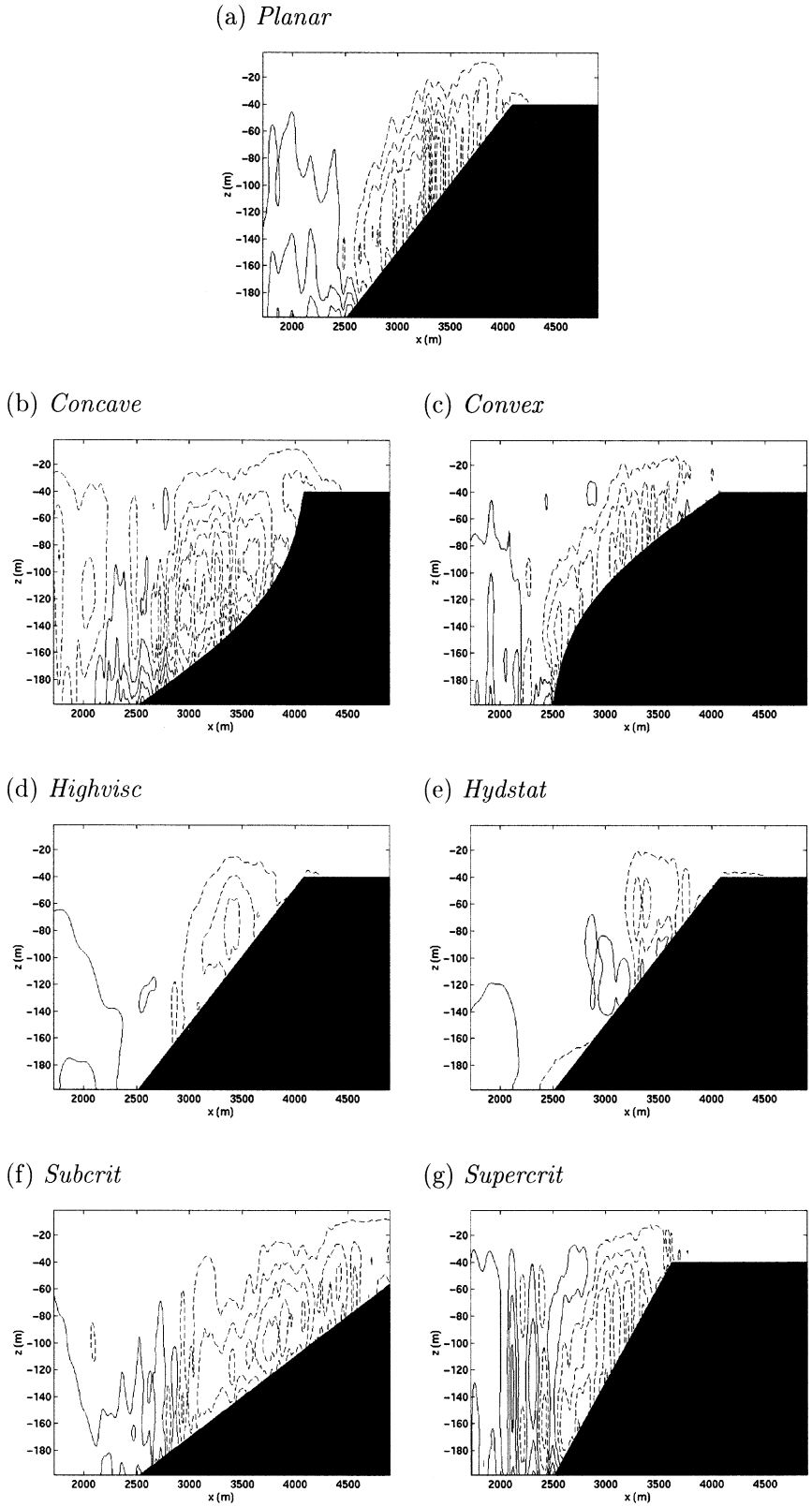

FIG. 16. Snapshots of buoyancy flux $\langle w'b' \rangle$ deduced from the net change in buoyancy over five tidal periods. The contour spacing is 5×10^{-10} m^2 s^{-3}, and dashed contours indicate negative values.

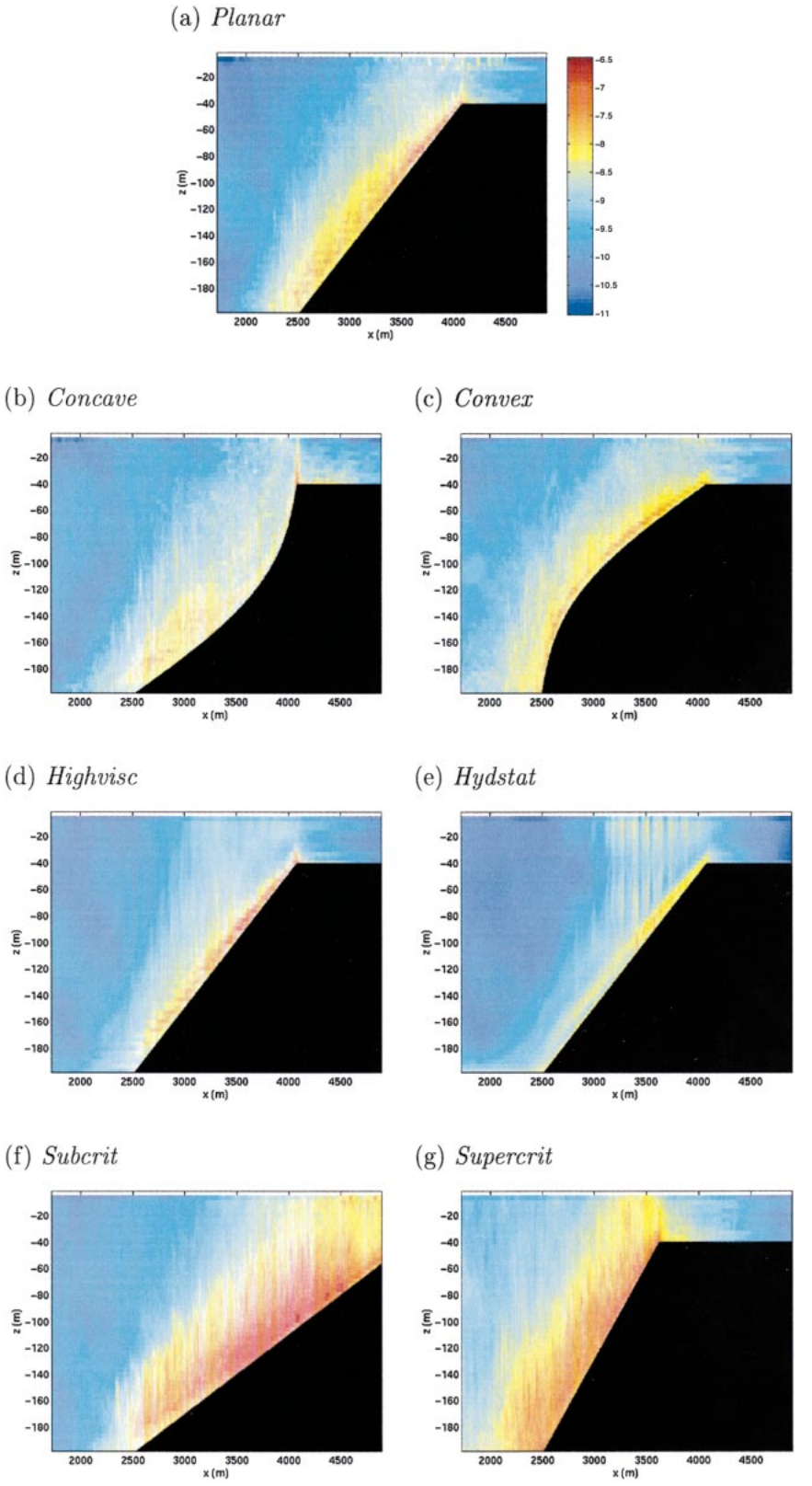

FIG. 17. Snapshots of net kinetic energy dissipation averaged over five tidal periods for (a) *Planar,* (b) *Concave,* (c) *Convex,* (d) *Highvisc,* (e) *Hydstat,* (f) *Subcrit,* and (g) *Supercrit.* The color scale is logarithmic and extends from 10^{-11} to $10^{-6.5}$ m^2 s^{-3}.

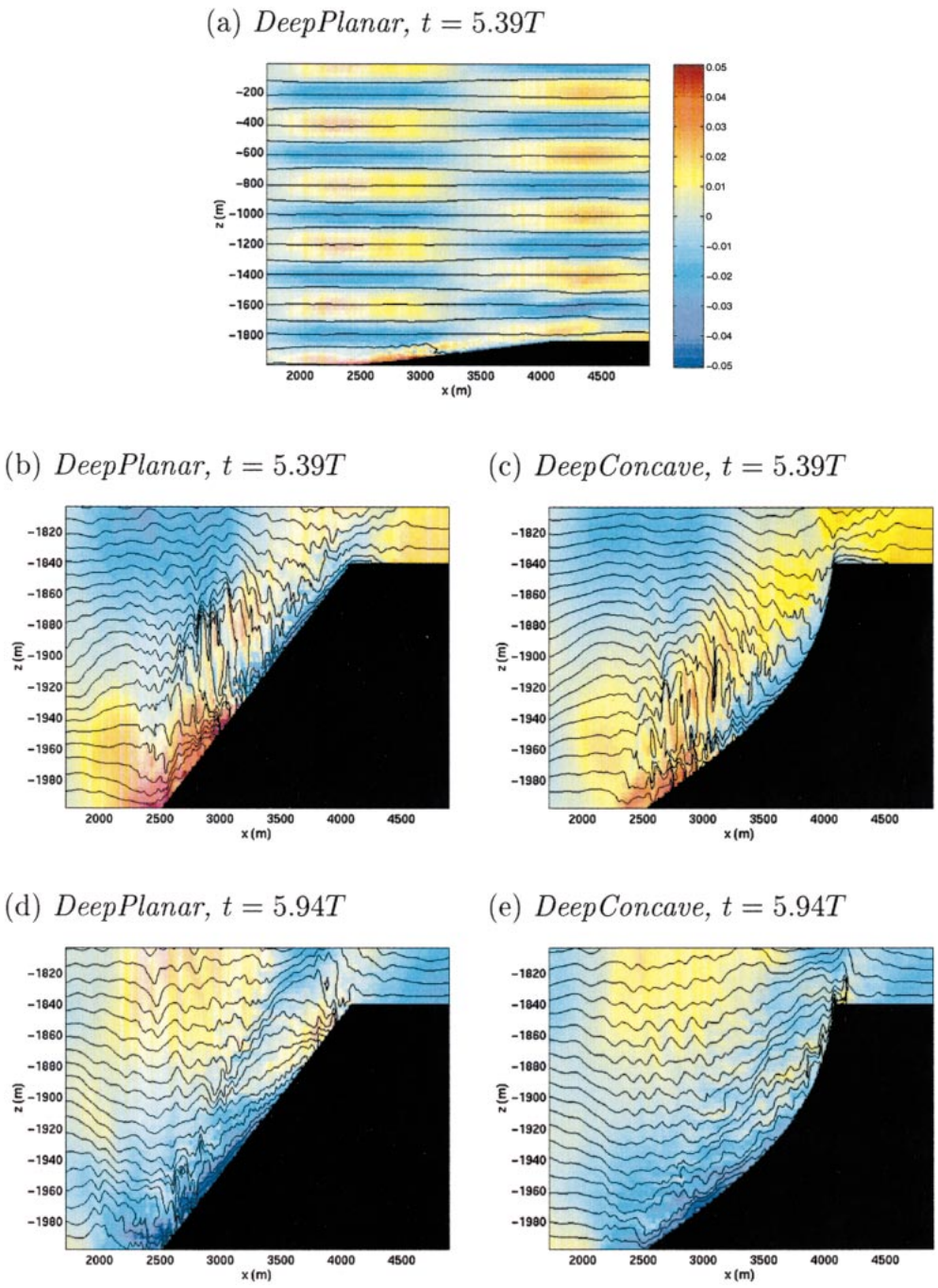

FIG. 18. Snapshots of cross-slope velocity (color) and buoyancy, for calculations of waves encountering a slope of height 160 m in a fluid of total depth 2000 m. The color scale extends between $U = -0.05$ m s^{-1} (blue) and $U = 0.05$ m s^{-1} (red), and the contour interval is $\Delta b = 9.81 \times 10^{-5}$ m s^{-2} in (a) and 9.81×10^{-6} m s^{-2} in (b)–(e).

0.053 and 0.057, respectively, as do *Subcrit* and *Supercrit.* Overall these are considerably smaller than values quoted by other authors (e.g., 30%, Slinn and Riley 1996), perhaps because our calculations are two-dimensional rather than three-dimensional. Furthermore, our dissipation Reynolds number $\mathrm{Re} = \epsilon/(\nu N^2)$ is a relatively small $O(1–10)$ for the low-viscosity calculations, so that we fall just at the edge of the stratified turbulence regime. (*Highvisc* and *Hydstat*, of course, have still lower Re and hence are not turbulent.) Often mixing efficiencies of 0.2 are assumed [e.g., in calculating diffusivities using the Osborn (1980) model], but

this only applies to highly turbulent, large-Re regimes (Itsweire et al. 1986).

d. Relative importance of shoaling as compared with critical reflection

Throughout this analysis we have focused on the reflection of the incoming internal wave from a slope near the critical angle as a cause of the wave breaking and mixing. However, in our simulations, there is a second important process—the shoaling of the wave due to the large decrease in total depth of the fluid. The probable importance of shoaling increases as $\Delta h/H \to 1$, where Δh is the total change in topographic height and H is the total depth. In the simulations discussed thus far, $\Delta h/H = 0.8$. Even for a slope that is far from critical, the energy density in a shoaling wave would be expected to increase significantly and perhaps lead to mixing. To ascertain whether shoaling is indeed the dominant process, we have performed two simulations of internal wave breaking in a fluid of depth $H = 2000$ m, with $\Delta h/H = 0.08$, where shoaling would not be expected to play an important role. The wavelength and frequency of the incoming wave, slope gradient, stratification, and horizontal resolution are kept as before. The vertical resolution is unchanged in the bottom 200 m (near the topography) and is coarser above. One simulation has planar slope (*DeepPlanar*), and the other slope has concave slope (*DeepConcave*).

Figure 18 shows snapshots of the cross-slope velocity and buoyancy for the two instants shown in Figs. 2 and 3. In Fig. 18a, the total depth of the fluid is shown for *DeepPlanar*, while the other snapshots show only the bottom 200 m near the slope. At $t = 5.39T$, both *DeepPlanar* and *DeepConcave* look very similar to their shallow counterparts, with bores on the lower half of the slope, accompanied by overturning. At $t = 5.94T$ there are some differences, when the bore reaches the top of the slope, principally the absence of the reverse front seen above the rear of the bore in the shallow calculations. Hence we conclude that shoaling is responsible for the depression of isopycnals following the bore but not for the initial bore formation and mixing. The stratification changes in the deep calculations are very similar to those seen in the shallow calculations and hence are not shown here. These deep calculations reinforce our interpretation of the wave breaking and mixing as being caused by the wave reflection from the slope.

4. Discussion: Reflection of finite-amplitude waves

Our calculations have demonstrated that the qualitative features of the flow such as the upslope propagating bores and the quantitative measures of mixing such as the buoyancy flux show little sensitivity to the shape of the slope. In contrast, Gilbert and Garrett (1989) predicted that at a locally concave critical point, energy density was likely to be less than at a locally convex critical point, and hence we might expect less mixing at the concave slope. One important difference between our calculations and the study of Gilbert and Garrett (1989) is that our calculations are highly nonlinear. We propose that the cancellation between up- and downslope-reflected waves predicted by Gilbert and Garrett (1989) does not occur because the reflection process is not symmetric about the critical point. This hypothesis is suggested by the comparison between the reflection at subcritical and supercritical planar slopes; in both cases, an upslope propagating bore is generated for finite-amplitude incoming waves. Previous analytic studies suggest that for finite-amplitude internal waves, a thermal front is created that propagates up the slope with the reflected wave phase velocity (Thorpe 1992). When the advective velocity exceeds the phase velocity, we would expect this thermal front to develop into a bore: a bore is an inherently nonlinear feature, typically with Froude number $\mathrm{Fr} > 1$. We therefore expect bores to form during reflection if the Froude number of the reflected wave is greater than 1.

The horizontal phase velocity of an internal wave is

$$(c_p)_h = \frac{\omega}{k}. \tag{22}$$

For specular reflection, the horizontal wavenumber of the reflected wave (Phillips 1977) is given by

$$k_R = k_I \frac{\sin(\beta + \theta)}{\sin(|\beta - \theta|)}, \tag{23}$$

where θ is the angle of the topography to the horizontal and β is the angle of the wave characteristic to the horizontal [$\tan(\beta) = s$]. The phase velocity is therefore slowed down on reflection (for $0 < |\beta - \theta| < \pi/2$),

$$(c_p)_R = \frac{\omega}{k_I} \frac{\sin(|\beta - \theta|)}{\sin(\beta + \theta)}. \tag{24}$$

From Phillips (1977) the velocity amplitude is increased upon reflection:

$$(U_0)_R = (U_0)_I \frac{\sin(\beta + \theta)}{\sin(|\beta - \theta|)}. \tag{25}$$

The Froude number of the reflected wave is therefore increased:

$$\mathrm{Fr}_R = \frac{(U_0)_R}{(c_p)_R} = \frac{(U_0)_I}{(c_p)_I}\left[\frac{\sin(\beta + \theta)}{\sin(|\beta - \theta|)}\right]^2. \tag{26}$$

We expect bores to be generated when $\mathrm{Fr} > 1$, and so we can determine a range of topographic angles $\theta_{C1} < \theta < \theta_{C2}$ for which bores will be generated, where θ_{C1} is subcritical and θ_{C2} is supercritical, given a particular amplitude and wavenumber of the incoming wave,

$$\tan(\theta_{C1}) = s\frac{\mathrm{Fr}_I^{-1/2} - 1}{\mathrm{Fr}_I^{-1/2} + 1} \quad \text{and}$$

$$\tan(\theta_{C2}) = s\frac{\mathrm{Fr}_I^{-1/2} + 1}{\mathrm{Fr}_I^{-1/2} - 1}, \tag{27}$$

where $\mathrm{Fr}_I = (U_0)_I/(c_p)_I$, the Froude number of the incoming wave. For our particular parameters $(c_p)_I = 8.88 \times 10^{-2}$ m s^{-1} and $(U_0)_I = 0.024$ m s^{-1}, giving $\mathrm{Fr}_I = 0.27$. Since $s = 0.101$ we have $\tan(\theta_{C1}) = 0.015$ and $\tan(\theta_{C2}) = 0.319$. Note that *Subcrit* and *Supercrit* fall well within these boundaries and, over most of the slope, *Convex* and *Concave* also have slopes within this range. The steepest slope in both *Convex* and *Concave* is $dh/dx = 0.47$, which is just outside this range, and from the numerical computations it appears that bores are indeed inhibited on the steepest parts of the slope.

Our calculations therefore suggest that mixing occurs for all shapes of slope that have slopes within the range likely to lead to $\mathrm{Fr}_R > 1$. No cancellation between waves reflected from above and below the critical point occurs for the concave slope because upon reflection density anomalies are advected up the slope as a bore, not propagated as a wave. Cancellation of reflected waves around a concave critical point might occur if the critical point were more of a corner, between a shallow lower slope ($\theta < \theta_{C1}$), and a steep upper slope ($\theta > \theta_{C2}$).

5. Conclusions

We have described a series of calculations of internal wave reflecting from a continental slope, with a variety of topographic slopes and shapes. In all cases we have found mixing associated with bores moving upslope followed by strongly sheared downflows. The mixing erodes stratification in a broad band above the slope, bounded by a region of increased stratification aligned with the wave characteristic slope. This mixing region can be associated with the region affected by the waves reflected from the slope. Eventually a quasi–steady state is reached, in which no further erosion of stratification occurs, with no further deepening of the partially mixed layer. It is important to note that our calculations are two-dimensional. In three dimensions the mixing processes themselves might be modified, and lateral transfer processes such as baroclinic instability might restratify the slope region (as in localized convection regions; Visbeck et al. 1996). Without an understanding of the efficiency of restratification processes, we cannot give an estimate of the time-averaged diffusivity resulting from the wave reflection and breaking process. Future work will also be necessary to determine the dependence on λ_x/L_h, the ratio of incoming horizontal wavelength to slope length scale, which has been held fixed in this study. The mixing may also be influenced by preexisting frictional bottom boundary layers, and background flows, not considered here.

We propose that the presence of mixing for all slope topographies, in contrast to earlier predictions of reduced mixing at concave slopes is a result of the nonlinearity of the reflected wave, which leads to the bore features, preventing a cancellation of waves reflected from above and below the critical point. Predictions of reflected wave Froude number seem to support this hypothesis. For any amplitude of incident wave, there will always be some range of slope angles around the critical angle with reflected Froude number $\mathrm{Fr} > 1$. An important question is whether for typical ocean parameters, the range θ_{C1}–θ_{C2} is a large one. If we consider the internal tides generated at the Mid-Atlantic Ridge, St. Laurent and Garrett (2002) predict a first-mode internal tide with amplitude $U_0 = 0.0018$ m s^{-1}. Using an average $N = 10^{-3}$ s^{-1} (same as the N used in our calculations) and depth $H = 4000$ m, then from Eq. (22) the Froude number of the first-mode internal tide is $\mathrm{Fr}_I = 0.001$. Then from Eq. (27) the range of slopes for which $\mathrm{Fr}_R > 1$ is $0.094 < dh/dx < 0.108$, which is small. Even for an internal wave amplitude that is an order of magnitude larger, $U_0 = 0.02$ m s^{-1}, $\mathrm{Fr}_I = 0.011$, and $\mathrm{Fr}_R > 1$ when $0.08 < dh/dx < 0.125$. The calculations described in this paper have a wider range of slopes leading to $\mathrm{Fr}_R > 1$ because of a larger Fr_I, which in turn results from the smaller depth (200 m instead of 4000 m) (hence larger m and smaller c_p). As stressed earlier, these results apply for internal waves at other frequencies too, and so it may be possible for the internal wave continuum to make as significant a contribution to the total mixing as the tidal-band internal waves.

If our 200-m-deep scenario had stratification more typical of the shallow coastal regions, where $N \sim 15 \times 10^{-3}$ s^{-1} (e.g., Nash and Moum 2001), then s would be reduced, as would Fr for a first-mode wave of the same velocity amplitude ($\mathrm{Fr}_I = U_0\pi s/H$). Hence the range of angles over which mixing might occur would also be less than seen in our simulations. However, coastal regions may also have greater wave velocities, thereby increasing Fr_I. To obtain mixing over a similar range of slopes as in these simulations, forcing would have to be $U_0 > 1$ m s^{-1} for this stronger stratification.

The study of internal wave breaking at topography is motivated by the desire to develop physically based parameterizations of tidal mixing. This study suggests that this particular aspect of tidal mixing could be parameterized by applying an enhanced diffusivity in a band above the slope whenever the slope angle falls within the range $\theta_{C1} < \theta < \theta_{C2}$, with the upper bound of the enhanced diffusivity coinciding with the wave characteristic. The Garrett–Munk spectrum could be used to prescribe the wave amplitude as a function of frequency and wavenumber, necessary to determine θ_{C1} and θ_{C2}.

Acknowledgments. We thank Carl Wunsch for useful discussions during the course of this work. Kurt Polzin, Eric Kunze, Greg Ivey, and two anonymous reviewers all provided constructive comments and suggestions that helped to improve the manuscript. Author Legg is fund-

ed by ONR Grant N0014-98-1-0096. Author Adcroft is funded by ONR/NOPP Grant N00014-99-1-1050.

REFERENCES

Adcroft, A., C. Hill, and J. Marshall, 1997: Representation of topography by shaved cells in a height coordinate ocean model. *Mon. Wea. Rev.,* **125,** 2293–2315.

Baines, P. G., 1982: On internal tide generation models. *Deep-Sea Res.,* **29,** 307–338.

Bell, T. H., 1975: Topographically generated internal waves in the open ocean. *J. Geophys. Res.,* **80,** 320–327.

Cacchione, D. A., and C. Wunsch, 1974: Experimental study of internal waves on a slope. *J. Fluid Mech.,* **66,** 223–239.

——, L. F. Pratson, and A. S. Ogston, 2002: The shaping of continental slopes by internal tides. *Science,* **296,** 724–727.

Dauxois, T., and W. R. Young, 1999: Near-critical reflection of internal waves. *J. Fluid Mech.,* **390,** 271–298.

Egbert, G. D., and R. Ray, 2000: Significant dissipation of tidal energy in the deep ocean inferred from satellite altimeter data. *Nature,* **405,** 775–778.

Eriksen, C., 1985: Implications of ocean bottom reflection for internal wave spectra and mixing. *J. Phys. Oceanogr.,* **15,** 1145–1156.

Gilbert, D., and C. Garrett, 1989: Implications for ocean mixing of internal wave scattering off irregular topography. *J. Phys. Oceanogr.,* **19,** 1716–1729.

Itsweire, E. C., K. N. Helland, and C. W. Van Atta, 1986: The evolution of grid-generated turbulence in a stably stratified flow. *J. Fluid Mech.,* **162,** 299–338.

Ivey, G. N., and R. I. Nokes, 1989: Vertical mixing due to the breaking of critical internal waves on sloping boundaries. *J. Fluid Mech.,* **204,** 479–500.

——, K. B. Winters, and I. P. D. de Silva, 2000: Turbulent mixing in a sloping benthic boundary layer energized by internal waves. *J. Fluid Mech.,* **418,** 59–76.

Khatiwala, S., 2003: Generation of internal tides in an ocean of finite depth: Analytical and numerical calculations. *Deep-Sea Res.,* **50,** 3–21.

Llewellyn Smith, S. G., and W. R. Young, 2002: Conversion of the barotropic tide. *J. Phys. Oceanogr.,* **32,** 1554–1566.

Marshall, J., A. Adcroft, C. Hill, L. Perelman, and C. Heisey, 1997: A finite-volume, incompressible Navier Stokes model for studies of the ocean on parallel computers. *J. Geophys. Res.,* **102,** 5753–5766.

Muller, P., and X. Liu, 2000a: Scattering of internal waves at finite topography in two dimensions. Part I: Theory and case studies. *J. Phys. Oceanogr.,* **30,** 532–549.

——, and ——, 2000b: Scattering of internal waves at finite topography in two dimensions. Part II: Spectral calculations and boundary mixing. *J. Phys. Oceanogr.,* **30,** 550–563.

Munk, W., and C. Wunsch, 1998: Abyssal recipes—II: Energetics of tidal and wind mixing. *Deep-Sea Res.,* **45,** 1977–2010.

Nash, J. D., and J. M. Moum, 2001: Internal hydraulic flows on the continental shelf: High drag states over a small bank. *J. Geophys. Res.,* **106,** 4593–4611.

Osborn, T. R., 1980: Estimates of the local rate of vertical diffusion from dissipation measurements. *J. Phys. Oceanogr.,* **10,** 83–89.

Phillips, O. M., 1977: *The Dynamics of the Upper Ocean.* 2d ed. Cambridge University Press, 336 pp.

Pietrzak, J., 1998: The use of TVD limiters for forward-in-time upstream-biased advection schemes in ocean modeling. *Mon. Wea. Rev.,* **126,** 812–830.

Polzin, K. L., 2004: Idealized solutions for the energy balance of the finescale internal wavefield. *J. Phys. Oceanogr.,* in press.

Slinn, D. N., and J. J. Riley, 1996: Turbulent mixing in the oceanic boundary layer caused by internal wave reflection from sloping terrain. *Dyn. Atmos. Oceans,* **24,** 51–62.

St. Laurent, L., and C. Garrett, 2002: The role of internal tides in mixing the deep ocean. *J. Phys. Oceanogr.,* **32,** 2882–2899.

Thorpe, S. A., 1992: Thermal fronts caused by internal gravity waves reflecting from a slope. *J. Phys. Oceanogr.,* **22,** 105–108.

——, M. Curé, and M. White, 1991: The skewness of temperature derivatives in oceanic boundary layers. *J. Phys. Oceanogr.,* **21,** 428–433.

Visbeck, M., J. Marshall, and H. Jones, 1996: Dynamics of isolated convective regions in the ocean. *J. Phys. Oceanogr.,* **26,** 1721–1734.

Winters, K., and E. D'Asaro, 1996: Diascalar flux and the rate of fluid mixing. *J. Fluid Mech.,* **317,** 179–193.

Wunsch, C., 1969: Progressive internal waves on slopes. *J. Fluid Mech.,* **35,** 131–145.